Viscoelastic Structural Damping Enables Broadband Low-Frequency Sound Absorption

Yanlin Zhang^{a,b}, Junyin Li^{b,c}, Qiongying Wu^d, Marco Amabili^b, Diego Misseroni^e, and Hanqing Jiang^{b,c,f*}

^aSchool of Materials Science and Engineering, Zhejiang University, Hangzhou 310027, China

^bSchool of Engineering, Westlake University, Hangzhou, Zhejiang 310030, China

^cWestlake Institute for Advanced Study, Hangzhou, Zhejiang 310024, China

^dZhejiang Sanlux Rubber Co. Ltd., Shaoxing, Zhejiang 312031, China

^eUniversity of Trento, 38123 Trento, Italy

^fResearch Center for Industries of the Future, Westlake University, Hangzhou, Zhejiang 310030,

China

*Email: hanging.jiang@westlake.edu.cn

Abstract

Low-frequency sound absorption has traditionally relied on air-resonant structures, such as

Helmholtz resonators, which are made of stiff materials that undergo negligible deformation. In

these systems, energy dissipation arises primarily from air motion and thermal-viscous effects,

resulting in inherently narrowband performance and bulky, complex designs for broadband

absorption. Here, we presented a composite acoustic metamaterial that replaces the high-stiffness

neck of a Helmholtz resonator with a soft, viscoelastic cylindrical shell. This structural

modification enables material deformation and shifts the dominant energy dissipation mechanism

from air resonance to intrinsic viscoelastic damping. A single unit achieves over 97% absorption

across a broad low-frequency range (227–329 Hz) with deep-subwavelength thickness (λ 15 at

227 Hz). We developed a discretized impedance model that quantitatively links material properties

and geometry to absorption behavior. Our results established a materials-centered design paradigm

in which both material selection and geometry serve as coequal, tunable parameters for compact,

broadband low-frequency sound control.

Keywords: Acoustic metamaterials; Low frequency; Broadband absorption; Viscoelastic damping;

Structural vibrations

2

Significance

Conventional acoustic metamaterials rely on air resonance and geometrically complex, high-stiffness structures to achieve low-frequency absorption, typically leading to negligible structural deformation. These approaches are inherently narrowband. We present a composite acoustic metamaterial that replaces the high-stiffness neck of a Helmholtz resonator with a soft, viscoelastic shell, shifting the dominant energy dissipation mechanism from air-based resonance to structural damping governed by material viscoelasticity. This transition enables over 97% absorption across a broad low-frequency band. A discretized impedance model links absorption performance to material and geometric parameters, establishing a predictive framework. This materials-centered approach reframes low-frequency acoustics by embedding damping into the material itself, demonstrating that both material selection and geometry serve as coequal ingredients for acoustic performance.

Introduction

Absorbing airborne sounds, particularly at low frequencies, is essential for controlling noise pollution and improving acoustic environments (1-3). Conventional porous materials achieve efficient absorption only when their thickness is comparable to a quarter of the acoustic wavelength (4, 5), which becomes impractically large at low frequencies. In response, acoustic metamaterials have attracted considerable attention over the past decade for enabling subwavelength absorption via engineered resonant structures (6-21). Example designs of these metamaterials include Helmholtz resonators (**Fig. 1A**) (13, 18, 22) that rely on air-column resonance within a high-stiffness neck whose deformation is negligible, Fabry-Pérot channels (15, 19, 21), and microperforated panels (20, 23, 24), which dissipate sound energy through air motion and associated thermal-viscous effects.

However, these air-resonant mechanisms remain inherently effective within a narrow frequency band. To broaden the absorption bandwidth, many recent efforts have combined heterogeneous resonators of varying scales, often at the cost of added complexity and volume (15-21). A smaller number of studies have looked beyond air resonance and explored the role of flexible structures. Membrane absorbers, for example, can enhance localized energy density and improve dissipation (25, 26), but they require precise control over membrane tension, making them environmentally sensitive, prone to instability, and difficult to tune (27). Other approaches include coupling flexible materials with open-air environments (28-30) or replacing the inner walls with soft materials (31-33), taking advantage of combined structural-acoustic modes to increase damping. However, these efforts often rely on parametric studies via simulations or experiments, with limited systematic theoretical frameworks. In most cases, absorption is still primarily driven by air movement rather than the material itself, necessitating complex multi-resonant assemblies for broadband performance.

This research gap leads to an opportunity. Soft materials, such as elastomers and gels, offer

distinctive advantages for acoustic applications, including low elastic modulus (ranging from a few kPa to some MPa), high intrinsic damping (loss tangent $\tan\delta\approx 0.1$ –1.0 or higher), and large deformability (34, 35). These properties are rarely used in acoustic systems. Still, they offer a fundamentally different route to low-frequency sound absorption: dissipating energy through material deformation, rather than mainly relying on air flow. Achieving this, however, requires more than a materials swap. It calls for an advanced theoretical approach. This theory must treat material dissipation, structural dynamics, and acoustic coupling as coequal components in the absorber's performance.

In this study, we introduced a composite acoustic metamaterial that replaces the high-stiffness neck of a traditional Helmholtz resonator (**Fig. 1A**) with a soft, viscoelastic cylindrical shell embedded within a sealed cavity (**Fig. 1F**). This simple structural change fundamentally alters the energy dissipation mechanism, from air-based resonance to structural damping governed by the material's intrinsic viscoelasticity. As a result, a single unit achieves over 97% absorption across a broad low-frequency range (227–329 Hz), with a deep-subwavelength thickness (λ /15 at 227 Hz). Furthermore, to understand and optimize this behavior, we developed a discretized impedance model that links the material properties (i.e., elastic modulus, loss factor, density) and geometry to absorption performance. We demonstrated that this model not only captures the observed behavior but also serves as a predictive tool for tuning absorption bands through material and structural design. More broadly, our approach reframes low-frequency acoustic design, namely, rather than relying on resonance stacking or complex architectures, we turn to the material itself as the dissipative medium. By integrating viscoelastic damping into the core architecture, we unlock a new class of compact, tunable, and broadband low-frequency sound absorbers, in which material choice, not just geometry, defines performance.

Results and Discussion

Rigid vs. Flexible-Neck Helmholtz Resonator

Traditional acoustic metamaterial absorbers often assume that the structural components, particularly the resonator neck, are made of materials with sufficiently high elastic moduli, so that their deformation under acoustic excitation is negligible. We refer to this class of systems as Rigid-Neck Helmholtz resonators (RN-Helmholtz resonators) throughout this work. As illustrated in Fig. 1A, an RN-Helmholtz resonator features a high-stiffness neck (Young's modulus E = 2,650MPa, density $\rho_s = 1{,}150 \text{ kg/m}^3$, loss factor $\eta = 0.01$) embedded in a sealed cavity. Incident sound waves propagate through the neck (indicated by white arrows), exciting resonance in the enclosed air column. Finite element simulations via COMSOL Multiphysics (see SI Appendix, Fig. S16 for details) were conducted to study the coupled acoustic-structural response of this system. As shown in **Fig. 1B**, the resulting air particle velocity distribution is concentrated within the neck region. Thus, the energy is primarily dissipated through thermal-viscous friction at the air-rigid neck boundaries, while the displacement of the neck is effectively vanishing (Fig. 1C). This mechanism confines significant absorption (defined by absorption coefficient $\alpha > 0.8$) to a narrow 18 Hz bandwidth (141-159 Hz) centered at the air column's resonance frequency (150 Hz, $\alpha = 0.999$) (Fig. 1D). To broaden the absorption bandwidth, multiple RN-Helmholtz resonators of varying dimensions (e.g., different cavity volumes and neck lengths) are inevitably combined (see SI Appendix, Fig. S17 for detailed geometries). The resulting multi-resonator structure (Fig. 1E) achieves significant absorption across a 210 Hz bandwidth (300–510 Hz), featuring five distinct absorption peaks (quantitative data in *SI Appendix*, Fig. S17). Consequently, this multi-resonator strategy increases structural complexity and poses challenges for fabrication, tuning, and integration.

In our work, we address these limitations by replacing the high-stiffness neck with a deformable, soft cylindrical shell (Young's modulus E = 120 kPa, density $\rho_s = 1{,}120$ kg/m³, loss factor $\eta = 0.4$)

(Fig. 1F). We refer to this configuration as the Flexible-Neck Helmholtz resonator (FN-Helmholtz resonator). Finite element simulations via COMSOL Multiphysics (see SI Appendix, Fig. S18 for details) were conducted to study the coupled acoustic-structural response of this system. In this configuration, incident sound waves propagate through the flexible neck region and also lead the soft shell to vibrate (indicated by blue arrows). On one hand, air-column resonance within the neck continues to contribute to energy dissipation (Fig. 1G). On the other hand, the soft shell undergoes substantial deformation (Fig. 1H), with displacement magnitudes three orders of magnitude higher than those of its high-stiffness counterpart (Fig. 1C), enabling efficient energy conversion through intrinsic viscoelastic damping. This shift in energy dissipation, from predominantly air-mediated losses to viscoelastic structural vibration, marks a fundamental departure from conventional Helmholtz resonator behavior. As a result, the FN-Helmholtz resonator achieves both broadband and high-efficiency sound absorption using a single unit, characterized by dual absorption peaks at 320 Hz ($\alpha = 0.974$) and 460 Hz ($\alpha = 0.967$) and a significant absorption with an adequate bandwidth spanning 215 Hz (294-509 Hz) (Fig. 11). Compared to broadband absorbers constructed from arrays of RN-Helmholtz resonators (yellow line in Fig. 1J, same as in Fig. 1E), this singleunit performance (blue line in Fig. 1J, same as in Fig. 1I) achieves a slightly wider effective bandwidth (215 Hz vs. 210 Hz), while eliminating the need for complex arrays of multi-resonator systems. The reduction in structural complexity, enabled by this materials-centered design, enhances manufacturability and establishes a compact, high-performance framework for lowfrequency acoustic absorption.

Experimental and Numerical Validation of Vibration-Induced Sound Absorption

To experimentally verify the simulation-based findings presented in the previous section, we fabricated an FN-Helmholtz resonator, consisting of a soft cylindrical shell and a rigid outer support structure (**Fig. 2A**). The soft shell was made from Ecoflex-30 silicone rubber (Smooth-On Inc., Young's modulus = 90 kPa), and the outer shell was 3D-printed using a photosensitive resin with a Young's modulus of 2,650 MPa. The detailed geometry is provided in the caption of **Fig.**

2A, and its fabrication process is outlined in *SI Appendix*, Fig. S13. Dynamic mechanical analysis (DMA 850, TA Instruments) was performed in compression mode to characterize the viscoelastic behavior of Ecoflex-30. Over the testing range, its storage modulus E and loss factor η approach approximately 148.5 kPa and 0.2, respectively, at high frequency (> 181 Hz) (Fig. 2B), as supported by time-temperature superposition (TTS) experiments (36), which extrapolated the data up to 596 Hz (see *SI Appendix*, Fig. S7 for details).

Normal-incidence sound absorption coefficients were measured using an acoustic impedance tube with an inner diameter of 29 mm (setup shown in *SI Appendix*, Fig. S14). The fabricated FN-Helmholtz resonator exhibited broadband absorption performance, featuring two prominent peaks at 330 Hz (α = 0.978) and 500 Hz (α = 0.996). Except for a dip in the mid-frequency range around 400 Hz (α = 0.677), the absorption coefficient remained above 0.8 over much of the range from 307 Hz to 535 Hz (Fig. 2C, blue). We also performed coupled acoustic–structural simulations using COMSOL Multiphysics (see *SI Appendix*, Fig. S19 for details) to compare with the experimental results, using the identical geometry and material properties as those of the experiment. The simulated absorption spectrum (Fig. 2C, orange) closely matched the experimental data, confirming the accuracy of the model and the broadband performance of the FN-Helmholtz resonator.

To elucidate the underlying sound absorption mechanism, we measured the surface vibration displacement of the cylindrical shell using a laser Doppler vibrometer (Polytec PSV-500). Scans of displacement amplitude and phase were conducted along three axial lines located at circumferential angles of 0°, 120°, and 240° on the shell surface (see *SI Appendix*, Fig. S15 for details). The results revealed nearly identical displacement profiles across the three directions (*SI Appendix*, Figs. S15D-G), indicating that the shell vibrates in an axisymmetric mode under acoustic excitation. Averaged experimental displacement data were compared with simulation results, showing good agreement in both amplitude and phase (Figs. 2D–G). In addition, the simulations directly visualized the axisymmetric vibration modes at two representative absorption

peaks (330 Hz and 500 Hz) (**Figs. 2H** and **2I**), with the displacement profiles matching well with the magnitude curves in **Figs. 2D** and **2E**, further confirming the mechanism.

Calculated distributions of dissipated power density (W/m³) at 330 Hz and 500 Hz (Figs. 2J and 2K) show that most of the energy dissipation occurs in the silicone rubber shell. We then integrated the power density over the rubber and air regions separately to obtain the total dissipated power (W) in each domain. The frequency-dependent results for both mechanisms are compared in Fig. 2L. Notably, the two prominent peaks in viscoelastic damping match well with the sound absorption peaks. This correlation confirms that the dominant energy loss in the composite absorber comes from the vibration-induced damping of the soft rubber, with a secondary contribution from air-related losses.

Equivalent Circuit Analysis of Acoustic-Structural Coupling

To quantitatively analyze the sound-structure interaction mechanism, we developed a discretized equivalent impedance model. As shown in Fig. 3A, this model discretizes the cylindrical shell and the enclosed air column into n equal-length segments (length = l/n) along the axial direction. Compared to the configuration in Fig. 2A, we omitted the outer shell thickness and focused only on the cavity boundary dimensions (see *SI Appendix*, Fig. S1 for detailed geometry). For each segment, the acoustic impedance of the air column, $Z_a(x_i)$, and the equivalent acoustic impedance of the flexible cylindrical shell, $Z_b(x_i)$, are connected in parallel, where $x_i = \frac{i}{n}l$ represents the position of the i^{th} (i = 1, 2, ..., n) segment along the shell axis. This setup captures the two primary paths of energy dissipation: sound traveling through the air column and structural vibrations within the shell. In addition, the enclosing cavity introduces a shared acoustic reactance Z_c , which is connected in series with the coupled impedance of the fluid-structure system. Figure 3B illustrates the complete acoustic impedance circuit diagram. The total acoustic response of the system is therefore governed by the combined effects of $Z_a(x_i)$, $Z_b(x_i)$, and Z_c . Detailed derivations of

these impedance components under clamped-free boundary conditions are provided in *SI*Appendix, Section 1.

A brief description is as follows. The total equivalent impedance, Z_e , of the system is calculated recursively. Starting from the n^{th} segment, the equivalent impedance T_n is determined by the parallel combination of $Z_n(x_n)$ and $Z_b(x_n)$, followed by a series connection with $Z_a(x_{n-1})$:

$$T_n = \frac{Z_a(x_n)Z_b(x_n)}{Z_a(x_n) + Z_b(x_n)} + Z_a(x_{n-1}).$$
[1]

For the preceding segments, the recursive relationship is expressed as:

$$T_{i-1} = \frac{T_i Z_b(x_{i-1})}{T_i + Z_b(x_{i-1})} + Z_a(x_{i-2}) \quad (i = n, n-1, ..., 3).$$
 [2]

This process continues iteratively up to the first segment, at which point the coupling impedance between the air column and the shell is fully determined:

$$T_{1} = \frac{T_{2}Z_{b}(x_{1})}{T_{2} + Z_{b}(x_{1})}.$$
 [3]

In addition, the acoustic reactance of the cavity, Z_c , is expressed as (37):

$$Z_c = -j \frac{\rho_0 c_0^2}{\omega V}, \tag{4}$$

where j is the imaginary number, V denotes the cavity volume, ρ_0 is the air density, c_0 is the sound speed, and ω is the angular frequency. Finally, the total equivalent impedance, Z_e , is given by:

$$Z_e = T_1 + Z_c. ag{5}$$

Assuming free boundary conditions at both ends of the cylindrical shell, the recursive model can be simplified to a closed-form analytical expression (see detailed derivation in *SI Appendix*, Section 2):

$$Z_e = \sqrt{Z_a Z_b} \tanh \sqrt{\frac{Z_a}{Z_b}} + Z_c.$$
 [6]

Here, Z_a the acoustic impedance of the air column, is derived by combining Crandall's theory (38) and Ingard's theory (22):

$$Z_{a} = \frac{1}{S_{a}} \left[\frac{-\mu k_{v}^{2} l}{1 - \frac{2}{k_{v} a} \frac{J_{1}(k_{v} a)}{J_{0}(k_{v} a)}} + 2\sqrt{2\mu\omega\rho_{0}} + j\omega\rho_{0}\delta \right],$$
 [7]

where μ is the air's dynamic viscosity, $k_v = \sqrt{\frac{-j\omega\rho_0}{\mu}}$ is the viscous wave number, a is the inner radius of the cylindrical shell, $S_a = \pi a^2$ is the air column's cross-sectional area, $2\sqrt{2\mu\omega\rho_0}$ represents the additional viscous loss at both shell ends, and $\delta = 0.85a\left(2 - 1.25\frac{a}{R}\right)$ is the end correction for acoustic mass (22). J_0 and J_1 are the 0^{th} and 1^{st} order Bessel functions of the first kind, respectively.

Similarly, Z_b , the shell's equivalent acoustic impedance (derived in **SI Appendix**, Section 2), is expressed as:

$$Z_{b} = \frac{Et}{2\omega\pi b^{3}l(1-v^{2})} \left[\eta + j \left(\frac{\omega^{2}\rho_{s}b^{2}(1-v^{2})}{E} - 1 \right) \right],$$
 [8]

where t is the shell thickness, $b = a + \frac{t}{2}$ is the mid-surface radius, E is the Young's modulus, η is the loss factor, ρ_s is the material density, and ν is the Poisson's ratio.

Notably, when the shell becomes rigid $(Z_b(x_i) \gg Z_a(x_i))$, the equivalent circuit reduces to the configuration shown in **Fig. 3C**, where the branches containing $Z_b(x_i)$ are effectively removed. Under this condition, Equation (6) reduces to a classical Helmholtz resonator model with impedance $Z_e = Z_a + Z_c$, validating the generality of the modeling framework.

The sound absorption coefficient α can then be calculated by its total acoustic impedance Z_e , using the following expression (39):

$$\alpha = 1 - \left| \frac{Z_e S - \rho_0 c_0}{Z_e S + \rho_0 c_0} \right|^2,$$
 [9]

where S is the cross-sectional area of the impedance tube $(S = \frac{\pi d^2}{4}, d)$ being the inner diameter of the tube), and $\rho_0 c_0$ is the characteristic impedance of air. This formula can also be conveniently rewritten in terms of the normalized acoustic resistance $x_s = \text{Re}\left(\frac{Z_e S}{\rho_0 c_0}\right)$ and normalized acoustic reactance $y_s = \text{Im}\left(\frac{Z_e S}{\rho_0 c_0}\right)$ as (37):

$$\alpha = \frac{4x_s}{(1+x_s)^2 + y_s^2}.$$
 [10]

It follows that when Z_e satisfies $Z_eS = \rho_0c_0$ (i.e., $x_s = 1$ and $y_s = 0$), the sound absorption coefficient reaches its maximum value, $\alpha = 1$.

The accuracy of the theoretical model was checked by comparing it with finite element simulation results (see *SI Appendix*, Fig. S20 for details). As shown in Figs. 3D–3F, the predicted absorption coefficient, normalized acoustic resistance, and reactance from the model match well with the simulation. Fig. 3G further compares the absorption coefficients obtained using the closed-form analytical model (Eq. 6, assuming free-free boundary conditions) and the full recursive model (assuming clamped-free boundary conditions). The differences between the two approaches are minor, suggesting that the simpler analytical model still captures the main behavior. Overall, this theoretical approach provides a direct connection between the material and geometric parameters of the shell and the resulting absorption response, which can be useful for guiding the design and optimization of flexible acoustic metamaterials.

Broadband Tunability of Sound Absorption

As mentioned in the previous section, achieving broadband, high-efficiency sound absorption relies on optimal impedance matching across a wide range of frequencies. The ideal scenario occurs when the normalized acoustic resistance $x_s \approx 1$ and the normalized acoustic reactance $y_s \approx 0$. These two conditions ensure that incident sound waves can efficiently enter the absorber (minimizing reflection) and that the material can dissipate acoustic energy effectively. To illustrate how such impedance matching can be achieved, we first introduce a baseline configuration for analysis, using the material and geometric parameters detailed in **Fig. 3** (E = 148.5 kPa, $\eta = 0.2$, $\rho_s = 1,070 \text{ kg/m}^3$, a = 4 mm, l = 35 mm, t = 1 mm, $V = 26746 \text{ mm}^3$, d = 29 mm). This baseline serves as a reference point for evaluating impedance characteristics and guiding optimization strategies.

Impedance Matching Strategy. The broadband performance of FN-Helmholtz resonator originates from the nonlinear, frequency-dependent coupling impedance $Z_{couple} = \sqrt{Z_a Z_b} \tanh \sqrt{\frac{Z_a}{Z_b}}$. Its normalized acoustic reactance, Im $\left(\frac{Z_{couple} S}{\rho_0 c_0}\right)$, displays a distinct Z-shaped profile (Fig. 4A, blue), featuring an inflection point at frequency f_p . A horizontal line passing through f_p intersects the curve at three points: f_{low} , f_p , and f_{high} , suggesting the potential for multimodal resonance (i.e., three crossings of the frequency axis). However, Z_{couple} alone is insufficient for achieving impedance matching, as the corresponding value of y_s along this line may still deviate considerably from the optimal condition $y_s = 0$.

To address this problem, the normalized cavity reactance, $Z_s^{cavity} = -j \frac{c_0 S}{\omega V}$, is introduced to act as a dynamic phase compensator by shifting the entire reactance curve downward along the imaginary axis (**Fig. 4A**, gray). By tuning the cavity volume V, the magnitude of this compensation can be precisely controlled, enabling the formation of an ideal bandwidth window (f_1, f_p, f_2) where $y_s = 0$ (**Fig. 4A**, green). The optimal cavity volume $V_{optimal}$ is determined by canceling the

reactance deviation at f_p , ensuring optimal compensation of the total reactance, i.e.,

$$\operatorname{Im}\left(\frac{Z_{couple}\left(\omega_{p}\right)S}{\rho_{0}c_{0}}\right) - \frac{c_{0}S}{\omega_{p}V_{optimal}} = 0.$$
 [11]

where $\omega_p = 2\pi f_p$ is the angular frequency corresponding to f_p .

Critically, although the normalized acoustic reactance y_s now crosses zero at three frequencies (f_1, f_p, f_2) , it retains its characteristic Z-shaped profile. Between these crossings, the curve deviates from zero: $y_s > 0$ for $f_1 < f < f_p$ and $y_s < 0$ for $f_p < f < f_2$ (**Fig. 4A**, green). At the same time, the normalized acoustic resistance x_s (**Fig. 4B**, green), dominated by $\operatorname{Re}\left(\frac{Z_{couple}S}{\rho_0c_0}\right)$, since the cavity impedance Z_s^{cavity} only contributes reactance, exhibits a pronounced peak at f_p , resulting in significant deviation from the ideal condition of $x_s = 1$. This simultaneous deviation in both y_s and x_s results in a noticeable dip in the absorption spectrum around the mid-frequency range (**Fig. 4C**, green).

To mitigate the mid-frequency dip, theoretical analysis demonstrates that replacing the constant loss factor ($\eta=0.2$, **Fig. 4D**, green) with a frequency-dependent function $\eta(f)=0.2+0.4 \exp\left(-\frac{\left(2\pi(f-f_p)\right)^2}{200000}\right)$, which peaks at the inflection frequency f_p (**Fig. 4D**, purple), offers an effective solution. This targeted modulation yields two synergistic effects: first, the increased damping flattens the Z-shaped curve of the normalized acoustic reactance y_s , forming a relatively flattened plateau (**Fig. 4A**, purple); second, the pronounced peak in the normalized acoustic resistance $x_s = Re\left(\frac{Z_e S}{\rho_0 c_0}\right)$ is substantially suppressed (**Fig. 4B**, purple). Together, these adjustments eliminate the mid-frequency dip and enable improved broadband absorption performance (**Fig. 4C**, purple). Importantly, this frequency-selective damping strategy is physically feasible, as it arises from viscoelastic relaxation mechanisms in soft materials. For instance, in gelatin-chitosan mixtures, tuning the gelatin molecular weight and temperature

controls polymer chain relaxation times, thereby dynamically adjusting the phase transition frequency (i.e., selective damping frequency) (34).

Parametric Study. To demonstrate the high tunability of the broadband absorber, we systematically investigated how key material properties (E, η, ρ_s) and geometric parameters (a, l, t, V, d) influence absorption performance. In this study, we varied one parameter at a time while holding the others constant. Notably, because the cavity volume V plays a critical role in impedance matching, it was dynamically adjusted according to Eq. 11 whenever another parameter was changed. This approach ensures that optimal impedance matching is maintained throughout the analysis, highlighting how V interacts with other design variables to influence the overall absorption characteristics.

Equation (8) shows that the natural frequency of the cylindrical shell is given by $\omega_0 = \sqrt{\frac{E}{\rho_s b^2 (1-\nu^2)}}$. This frequency defines the operational region in which the shell's vibrational modes can strongly couple with acoustic waves. Therefore, reducing the Young's modulus E (Fig. 4E), increasing material density ρ_s (Fig. 4F), or enlarging the mid-surface radius b (where $b=a+\frac{t}{2}$, modulated by radius a in Fig. 4G) can shift the impedance-matching region toward lower frequencies. However, these modifications require a corresponding increase in the optimal cavity volume $V_{optimal}$ to mantain effective dynamic phase compensation (Figs. 4E-G).

In addition to the frequency-selective damping strategy discussed earlier, uniformly increasing the constant loss factor η across all frequencies can also enhance overall absorption performance (**Fig.** 4H). However, this approach reduces the required optimal cavity volume $V_{optimal}$ needed to maintain effective phase compensation. Increasing the shell length l shifts the first absorption peak toward lower frequencies, with minimal impact on the second peak (**Fig. 4I**). In contrast, increasing the shell thickness t primarily lowers the second absorption peak while leaving the first

peak largely unchanged (**Fig. 4J**). This decoupled influence allows for independent fine-tuning of the two absorption peaks.

By jointly tuning material properties (E, η, ρ_s) and geometric parameters (a, l, t), along with dynamic phase compensation through the cavity volume V, the system's acoustic impedance can be synergistically optimized to achieve enhanced and highly customizable performance across target frequency ranges.

In contrast, increasing the cavity volume V alone, without coordinated adjustments to other parameters, can shift the absorption spectrum toward lower frequencies but may degrade performance due to impedance mismatch (**Fig. 4K**). Likewise, simply enlarging the cross-sectional area S of the impedance tube (modulated by tube diameter d in **Fig. 4L**) can worsen impedance mismatch and reduce absorption efficiency, as the absorber must dissipate energy over a larger area. These results underscore the importance of system-level optimization: isolated parameter changes are insufficient for maintaining impedance balance and achieving strong, broadband absorption.

Experimental Implementation: Material Optimization and Customized Absorber Designs

To validate the predictive capability of the theoretical model, we experimentally optimized the viscoelastic properties of silicone rubber and adjusted geometric parameters for customized low-frequency absorption. Specifically, we selected a softer silicone rubber (Ecoflex-20, Smooth-On Inc.) as the base material. By altering the prepolymer mixing ratio (A:B = 1:2 by mass) and introducing tungsten (W) powder (particle size <1 μ m) as a density-enhancing filler, we prepared two material variants: (1) a low-modulus, high-damping rubber (Ecoflex-20, A:B = 1:2) and (2) a density-enhanced composite (Ecoflex-20 + W, A:B:W = 1:2:1.2).

Dynamic mechanical analysis (DMA) in compression mode showed that both materials exhibited frequency-dependent viscoelastic behavior (**Figs. 5A** and **5B**). The storage modulus increased with frequency and stabilized at approximately 111 kPa, representing a 25.3% reduction compared to Ecoflex-30's 148.5 kPa. Meanwhile, the loss factor rose significantly to 0.385, marking a 92.5% increase over Ecoflex-30's value of 0.2. Importantly, the addition of W powder had minimal effect on the storage modulus and loss factor but markedly increased the material density from 1,070 kg/m³ to 1,420 kg/m³ (**Fig. 5C**). This ability to independently tune viscoelasticity and density underscores the flexibility of material design in achieving targeted acoustic performance.

Three absorber sets were developed to exploit the improved material properties:

Set 1 used Ecoflex-20 and coordinated shell dimensions (inner radius a = 4 mm, length l = 41.5 mm, thickness t = 1 mm), paired with a compensatory cavity height (h = 63 mm) to accommodate the material's lower stiffness. Experimental measurements (**Fig. 5D**, blue) demonstrated broadband absorption from 260–470 Hz (defined by $\alpha > 0.83$), with an average absorption coefficient of 0.912 (computed as the arithmetic mean over this range). This downward shift from the original design (307–535 Hz, **Fig. 2C**) validates the model's sensitivity to modulus reduction (**Fig. 4E**).

Set 2 adopted the density-enhanced Ecoflex-20+W composite, while keeping the exact shell dimensions as Set 1. To compensate for the higher density, the cavity height was increased to h = 72 mm. As a result, the absorption band (defined by $\alpha > 0.9$) shifted further to 248–405 Hz (**Fig. 5E**, blue), with an average coefficient of 0.949, aligning with the predicted density-dependent shift (**Fig. 4F**).

Set 3 also employed the Ecoflex-20 + W composite but enlarged the shell dimensions (a = 4.5 mm, l = 50 mm, t = 1.5 mm) and expanded the cavity height to h = 100 mm. This setup achieved near-perfect absorption from 227–329 Hz (defined by $\alpha > 0.97$) (**Fig. 5F**, blue), with an average coefficient of 0.986, while maintaining an overall thickness of just 1/15 of the wavelength at

227 Hz.

Experimental results from all three sets showed excellent agreement with numerical simulations (**Figs. 5D–F**, orange curves). This consistency was further supported by the validation of normalized acoustic resistance and reactance, presented in *SI Appendix*, **Fig. S21**, reinforcing the robustness of the theoretical model in capturing the relationship between material properties, structural parameters, and acoustic performance. Together, these findings demonstrate a closed-loop workflow that seamlessly integrates theoretical modeling, material formulation, structural design, and experimental validation.

Discussion

This work introduces a new strategy for achieving efficient low-frequency and broadband sound absorption by rethinking the role of structural materials in acoustic metamaterials. Traditional Helmholtz resonators rely on rigid components, with energy loss coming mainly from air motion and thermo-viscous effects, which limits them to narrow frequency bands. In contrast, our design replaces the rigid neck with a soft, viscoelastic cylindrical shell, allowing the structure itself to participate in the energy dissipation process through material damping and structural vibration. This shift enables a single resonator unit to achieve over 97% absorption across a tunable low-frequency range (e.g., 227–329 Hz), with a thickness as small as 1/15 of the wavelength at the lowest frequency.

The broadband performance arises from the combined effects of the shell's viscoelastic behavior and its dynamic interaction with the surrounding air. We developed a discretized impedance model to describe this coupled system, which enables us to directly link material properties (such as modulus, damping, and density) and geometric parameters (including shell radius, length, and thickness) to acoustic performance. Notably, shell length and wall thickness offer decoupled control over the position of absorption peaks, while material properties can be independently tuned

using mixing ratios or fillers. This provides the system with a high degree of flexibility in meeting various design goals.

The concept of embedding the damping mechanism into the structure itself, rather than relying solely on air resonance, opens the door to more compact, lightweight, efficient, and tunable absorbers. The approach also offers a practical path forward, utilizing common soft materials such as silicone rubber and straightforward fabrication methods. More broadly, it suggests that the conventional reliance on rigid structures and complex multi-resonator assemblies for broadband performance may not be necessary. Instead, a materials-centered framework, where viscoelastic properties are deliberately engineered and matched with structural geometry, can achieve high-performance absorption in a simpler, more compact, and lightweight form.

Looking ahead, this design approach could be extended to systems with multiple degrees of freedom, layered or hierarchical structures, or active tunability through external stimuli like temperature or electric fields. The same principle of structure-enabled dissipation also holds promise in underwater acoustics. Furthermore, this concept also has potential applications beyond acoustic absorption, such as in vibration damping, wave filtering, or programmable mechanical metamaterials. By combining ideas from material science, mechanics, and wave physics, this work lays the groundwork for a new class of flexible, efficient sound-absorbing materials suited to the needs of dense urban areas, transportation systems, and industrial noise control.

Acknowledgement

We thank the Research Center for Industries of the Future (RCIF) at Westlake University, Zhejiang Sanlux Rubber Co. ltd., and the Westlake Education Foundation for their support of this work. H.J. acknowledges support from the National Natural Science Foundations of China (Grants 12350003). D.M acknowledges financial support from the European Union, ERC grant HE GA 101086644 S-FOAM. (Views and opinions expressed are however those of the author(s) only and do not necessarily reflect those of the European Union or the European Research Council Executive Agency. Neither the European Union nor the granting authority can be held responsible for them), and the Westlake Fellows program. We thank Zhen Yang from Instrumentation and Service Center for Physical Sciences at Westlake University for her assistance with the DMA test and data interpretation.

Author contributions

Y.Z., Q.W. and H.J. designed research; Y.Z. and J.L. performed research; Y.Z., J.L., D.M., and H.J. analyzed data; and Y.Z., D.M., M.A., and H.J. wrote the paper.

Data availability

Source data for all main and supplementary figures are provided in the accompanying Excel file. MATLAB code for calculating the sound absorption coefficient (including Full-recursive and Closed-form analytical models) is available in the GitHub repository (https://github.com/yanlinZhang865/Data-availability).

Materials and Methods

Material Preparation and Fabrication

Flexible cylindrical shells were fabricated using silicone rubbers (Ecoflex-30 and Ecoflex-20, Smooth-On Inc.). Ecoflex-30 was prepared by mixing prepolymers (Part A:B) at a 1:1 mass ratio, while Ecoflex-20 was prepared at a 1:2 ratio (Part A:B) to reduce stiffness and enhanced damping. For density modification, tungsten (W) powder (particle size <1 μm) was added to Ecoflex-20 prepolymers at a mass ratio of A:B:W = 1:2:1.2. The mixed prepolymers were then cast into high-precision CNC-machined aluminum molds (see *SI Appendix*, Figs. S13A-D for details) and cured at 25 °C for 4 hours. After curing, the silicone cylindrical shell was demolded and trimmed to its final dimensions (see *SI Appendix*, Fig. S13E). The fabricated shells exhibited excellent dimensional fidelity, with deviations of less than 0.05 mm from the design specifications. The high-stiffness outer shell was fabricated using 3D printing (photosensitive resin, C-UV9400A, Young's modulus: 2,650 MPa). The soft silicone rubber shell was then embedded into the resin shell and bonded using silicone adhesive (Sil-Poxy, Smooth-On Inc.), forming a complete composite absorber (see *SI Appendix*, Fig. S13F). For visual clarity, in Fig. 2A, Figs. 5D-F and *SI Appendix*, Fig. S13F, we depict the outer shells as transparent acrylic (PMMA) to reveal the internal structure, although the actual fabricated shells were opaque.

Experimental Characterization

DMA.

Viscoelastic properties (storage modulus and loss factor) were measured using a TA Instruments DMA 850 analyzer in compression mode (experimental setup and sample geometry shown in *SI Appendix*, Fig. S7). Square samples (18 × 18 × 6 mm³) were tested under frequency sweeps (1–181 Hz, 10 Hz intervals) at 0.5% strain and 25°C. The dimensions of the square samples were chosen to minimize data fluctuations at higher frequencies (> 100 Hz). Comparisons with alternative testing methods (time-temperature superposition and cantilever beam resonance

method) are discussed in detail in SI Appendix, Section 4.

Sound Absorption Measurement.

Normal-incidence sound absorption coefficients were measured using an impedance tube (AWA6290T Hangzhou Aihua Instruments Co., inner diameter: d = 29 mm) following ISO 10534-2 standards. The experimental setup is shown in *SI Appendix*, Fig. S14. A 110 dB white noise signal (50-6300 Hz) served as the excitation sound source. Acoustic responses were recorded by two microphones, and absorption coefficients were calculated using the transfer function method (40). Due to the low stiffness of the flexible cylindrical shell, horizontal sample orientation induced slight gravitational sagging (see *SI Appendix*, Fig. S14B). To eliminate this effect, the impedance tube was reoriented vertically (*SI Appendix*, Fig. S14C), minimizing structural deflection during testing. Comparative analysis of absorption spectra from both horizontal and vertical configurations (*SI Appendix*, Fig. S14D) showed nearly identical results with overlapping curves, confirming that gravitational sagging negligibly impacted acoustic performance under the tested sample conditions.

Vibration Displacement Measurement.

Surface vibration displacement of the cylindrical shell under acoustic excitation at 330 Hz and 500 Hz was measured using a Polytec-PSV-500 laser Doppler vibrometer (experimental setup shown in *SI Appendix*, Fig. S15A). To ensure unobstructed laser access to the shell surface, the sample was enclosed in a transparent acrylic enclosure with a rectangular cross-section (*SI Appendix*, Fig. S15B). This design minimized spurious laser reflections from the curved cylindrical surface. The rectangular enclosed cavity volume was designed to match the cylindrical cavity volume designed in Fig. 2A. Axial vibration profiles were scanned along three axial lines at angular positions of 0° , 120° , and 240° (*SI Appendix*, Fig. S15C) with a spatial resolution of 0.2 mm (along *x* axis) to evaluate vibration symmetry. The measured displacement amplitudes and phase angles at both

excitation frequencies (330 Hz and 500 Hz) exhibited consistent spatial distributions across all angular orientations (*SI Appendix*, Figs. S15D-G), confirming the axisymmetric vibration behavior of the cylindrical shell.

Numerical Simulations

Coupled acoustic-structural simulations were performed in COMSOL Multiphysics (version 6.1) using the *Pressure Acoustic, Thermo-viscous Acoustics and Solid Mechanics modules* (*SI Appendix*, Fig. S19B). The resin shell was modeled as rigid, while the air domain was treated as a thermos-viscous fluid. All silicone rubbers were assumed to be nearly incompressible (Poisson's ratio: 0.49). A perfectly matched layer (PML) boundary condition was applied at the tube outlet to eliminate wave reflections. The computational domain was discretized using hexahedral meshes, with boundary layer meshes further refined in thermo-viscous region. Boundary conditions included fixed constraints at the silicone-resin interface and acoustic-structure coupling at the solid-air interface.

Viscoelastic damping in silicone rubber was quantified by integrating the dissipated power density (*solid.Qh*, W/m³) over the rubber domain. Similarly, thermo-viscous losses in air domains (resonator cavity and adjacent tube section) were evaluated by integrating the corresponding dissipation density (*ta.diss tot*, W/m³) over fluid volumes.

Stability of Sound Absorption Performance

Long-term Stability.

The FN-Helmholtz resonator sample (Set 3, **Fig. 5F**) was stored at 25°C ambient conditions and re-tested after 60 days and 80 days. The absorption coefficient, normalized acoustic resistance, and normalized acoustic reactance were measured using the same impedance tube setup. The comparative results are presented in *SI Appendix*, **Fig. S9**.

Temperature Effects.

To evaluate temperature influence on Ecoflex-30 viscoelastic properties and acoustic performance of the FN-Helmholtz resonator, temperature-dependent data from time-temperature superposition experiments were analyzed. Coupled acoustic-structural simulations compared absorption spectra at 25°C (E = 152 kPa, $\eta = 0.19$) and -10°C (E = 169 kPa, $\eta = 0.22$). Results (*SI Appendix*, Fig. S10) show relatively stable broadband absorption across a wide temperature range.

Absorption Under Oblique Incidence.

To assess performance under non-normal incidence, absorption coefficients were calculated for angles of 0°, 30°, and 60° using the full recursive model with clamped-free boundaries. For a locally reacting surface, the absorption coefficient $\alpha(\theta)$ is calculated by modifying the formula (Eq. 9) to account for the effective impedance projection along the direction of propagation (5):

$$\alpha(\theta) = 1 - \left| \frac{Z_e S \cos \theta - \rho_0 c_0}{Z_e S \cos \theta + \rho_0 c_0} \right|^2.$$
 [12]

where θ is the incidence angle measured from the normal to the surface. The resulting spectra (*SI Appendix*, Fig. S11) show angle-dependent variations.

Absorption Under High Sound Pressure. To evaluate potential influences of geometric or material nonlinearity at elevated incident sound levels, the normal-incidence sound absorption coefficient of the fabricated FN-Helmholtz resonator was measured under white-noise excitation at 90-129 dB (0.632-56.2 Pa). All curves are nearly identical across this range of incident sound pressures (*SI Appendix*, Fig. S12), this indicates that the absorber operates linearly even at high excitation levels. Moreover, simulations show maximal shell strain ≤ 1.44% at 129 dB (*SI Appendix*, Table S2), within Ecoflex-30's linear regime (<10% strain) (41). These results support the validity of the linear model used in our study.

Reference

- [1] G. Ma, P. Sheng, Acoustic metamaterials: From local resonances to broad horizons. Sci. Adv. 2, e1501595 (2016).
- [2] M. Yang, P. Sheng, Sound absorption structures: From porous media to acoustic metamaterials. Annu. Rev. Mater. Res. 47, 83–114 (2017).
- [3] S. Huang, et al., Sound-absorbing materials. Phys. Rev. Appl. 20, 010501 (2023).
- [4] L. Cao, et al., Porous materials for sound absorption. Compos. Commun. 10, 25–35 (2018).
- [5] J. Allard, N. Atalla, Propagation of sound in porous media: Modelling sound absorbing materials. (John Wiley & Sons, 2009).
- [6] S. A. Cummer, J. Christensen, A. Alù, Controlling sound with acoustic metamaterials. Nat. Rev. Mater. 1, 1–13 (2016).
- [7] N. Gao, et al., Acoustic metamaterials for noise reduction: A review. Adv. Mater. Technol. 7, 2100698 (2022).
- [8] S. Qu, P. Sheng, Microwave and acoustic absorption metamaterials. Phys. Rev. Appl. 17, 047001 (2022).
- [9] M. Yang, P. Sheng, Acoustic metamaterial absorbers: The path to commercialization. Appl. Phys. Lett. 122, 26 (2023).
- [10] B. M. Assouar, et al., Acoustic metasurfaces. Nat. Rev. Mater. 3, 460–472 (2018).
- [11] Y. Li, B. M. Assouar, Acoustic metasurface-based perfect absorber with deep subwavelength thickness. Appl. Phys. Lett. 108, 6 (2016).
- [12] N. Jiménez, et al., Ultra-thin metamaterial for perfect and quasi-omnidirectional sound absorption. Appl. Phys. Lett. 109, 12 (2016).
- [13] S. Huang, et al., Acoustic perfect absorbers via Helmholtz resonators with embedded apertures.

 J. Acoust. Soc. Am. 145, 254–262 (2019).
- [14] K. Donda, et al., Extreme low-frequency ultrathin acoustic absorbing metasurface. Appl. Phys.

- Lett. 115, 17 (2019).
- [15] M. Yang, et al., Optimal sound-absorbing structures. Mater. Horiz. 4, 673–680 (2017).
- [16] C. Zhang, X. Hu, Three-dimensional single-port labyrinthine acoustic metamaterial: Perfect absorption with large bandwidth and tunability. Phys. Rev. Appl. 6, 064025 (2016).
- [17] N. Jiménez, et al., Rainbow-trapping absorbers: Broadband, perfect and asymmetric sound absorption by subwavelength panels for transmission problems. Sci. Rep. 7, 13595 (2017).
- [18] S. Huang, et al., Compact broadband acoustic sink with coherently coupled weak resonances. Sci. Bull. 65, 373–379 (2020).
- [19] L. Liu, et al., Broadband acoustic absorbing metamaterial via deep learning approach. Appl. Phys. Lett. 120, 25 (2022).
- [20] C. R. Liu, et al., Ultra-broadband acoustic absorption of a thin microperforated panel metamaterial with multi-order resonance. Compos. Struct. 246, 112366 (2020).
- [21] C. Liu, et al., Ultra-broadband acoustic absorption with inhomogeneous high-order Fabry–P érot resonances. APL Mater. 11, 10 (2023).
- [22] U. Ingard, On the theory and design of acoustic resonators. J. Acoust. Soc. Am. 25, 1037–1061 (1953).
- [23] C. Wang, et al., Sound absorption of a micro-perforated panel backed by an irregular-shaped cavity. J. Acoust. Soc. Am. 127, 238–246 (2010).
- [24] D. -Y. Maa, Potential of microperforated panel absorber. J. Acoust. Soc. Am. 104, 2861–2866 (1998).
- [25] J. Mei, et al., Dark acoustic metamaterials as super absorbers for low-frequency sound. Nat. Commun. 3, 756 (2012).
- [26] G. Ma, et al., Acoustic metasurface with hybrid resonances. Nat. Mater. 13, 873–878 (2014).
- [27] T.-Y. Huang, C. Shen, Y. Jing, Membrane-and plate-type acoustic metamaterials. J. Acoust.

- Soc. Am. 139, 3240–3250 (2016).
- [28] S. S. Nudehi, G. S. Duncan, U. Farooq, Modeling and experimental investigation of a Helmholtz resonator with a flexible plate. J. Vib. Acoust. 135, 041102 (2013).
- [29] S. Cui, R. L. Harne, Soft materials with broadband and near-total absorption of sound. Phys. Rev. Appl. 12, 064059 (2019).
- [30] R. Tsuruta, et al., Reconfigurable acoustic absorber comprising flexible tubular resonators for broadband sound absorption. Phys. Rev. Appl. 18, 014055 (2022).
- [31] F. Ma, et al., Enhancing of broadband sound absorption through soft matter. Mater. Horiz. 9, 653–662 (2022).
- [32] P. Sun, et al., Sound absorption of space-coiled metamaterials with soft walls. Int. J. Mech. Sci. 261, 108696 (2024).
- [33] X. Liu, et al., Vibro-acoustic Helmholtz absorber with soft wall for broadband sound absorption. Int. J. Mech. Sci. 289, 110083 (2025).
- [34] B. Park, et al., Cuticular pad-inspired selective frequency damper for nearly dynamic noise–free bioelectronics. Sci. 376, 624–629 (2022).
- [35] S. Yang, P. Sharma, A Tutorial on the Stability and Bifurcation Analysis of the Electromechanical Behavior of Soft Materials. Appl. Mech. Rev. 75, 044801 (2023).
- [36] Y. Ding, A. P. Sokolov, Breakdown of time-temperature superposition principle and universality of chain dynamics in polymers. Macromolecules 39, 3322–3326 (2006).
- [37] G. Du, Z. Zhu, X. Gong, Fundamentals of Acoustics. 3rd ed. (Nanjing University Press, 2012).
- [38] I. B. Crandall, Theory of vibrating systems and sound. (D. Van Nostrand Company, 1926).
- [39] P. M. Morse, K. U. Ingard, Theoretical acoustics. (Princeton University Press, 1986).
- [40] J. Y. Chung, D. A. Blaser, Transfer function method of measuring in-duct acoustic properties.
- I. Theory. J. Acoust. Soc. Am. 68, 907–913 (1980).
- [41] C. Romano, et al., Tunable soft pressure sensors based on magnetic coupling mediated by

Figures

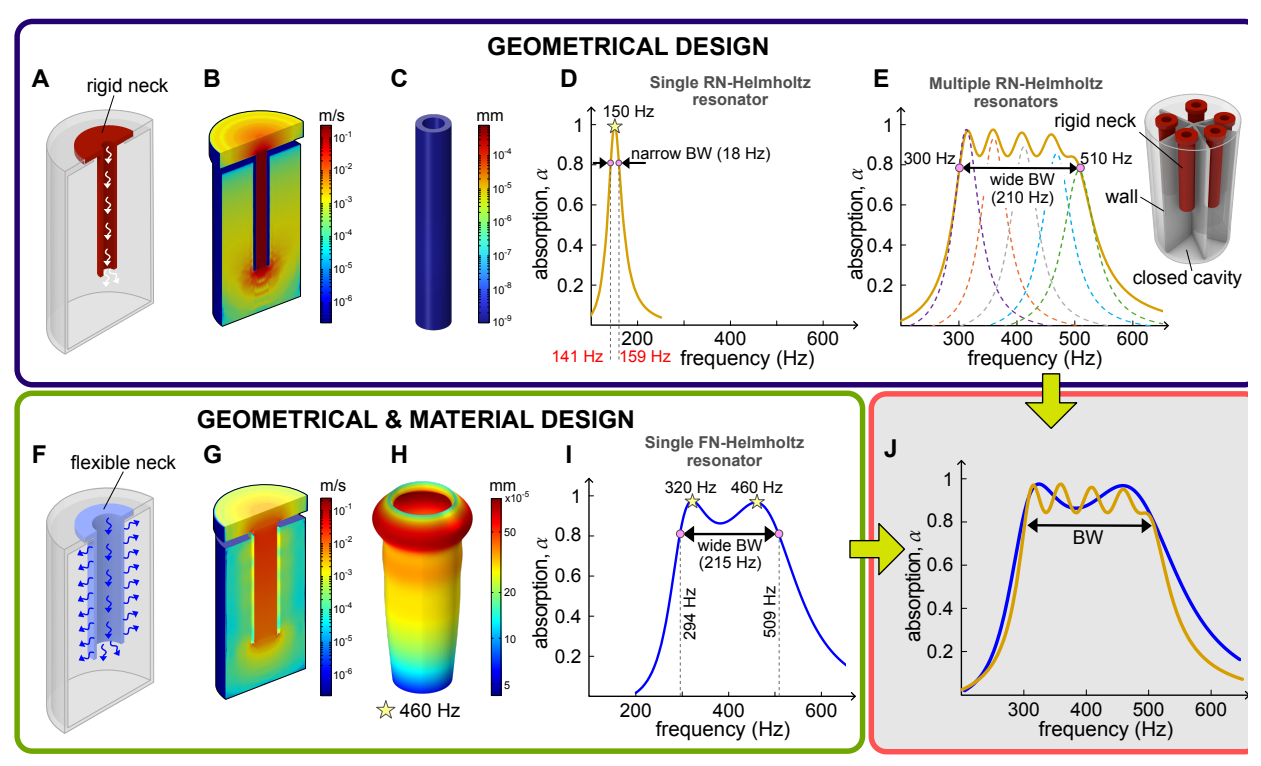


Fig. 1. Rigid vs. Flexible-Neck Helmholtz Resonators: Mechanisms and Performance. (A) Cross-sectional schematic of a conventional Rigid-Neck Helmholtz resonator (RN-Helmholtz resonator). (B) Simulated air particle velocity distribution in the RN-Helmholtz resonator at resonance frequency (150 Hz). (C) Displacement field of the RN-Helmholtz resonator neck at 150 Hz. (D) Sound absorption coefficient of the single RN-Helmholtz resonator. (E) Sound absorption coefficient of Multiple RN-Helmholtz resonators comprising five units. (F) Cross-sectional schematic of the Flexible-Neck Helmholtz Resonator (FN-Helmholtz resonator). (G) Air particle velocity distribution in the FN-Helmholtz resonator at 460 Hz. (H) Displacement field of the FN-Helmholtz resonator neck at 460 Hz (displacement magnified ×5000 for visibility). (I) Sound absorption coefficient of the single FN-Helmholtz resonator. (J) A comparison of absorption coefficients between Multiple RN-Helmholtz resonators (marked in yellow) and the single FN-Helmholtz resonator (marked in blue). BW: bandwidth.

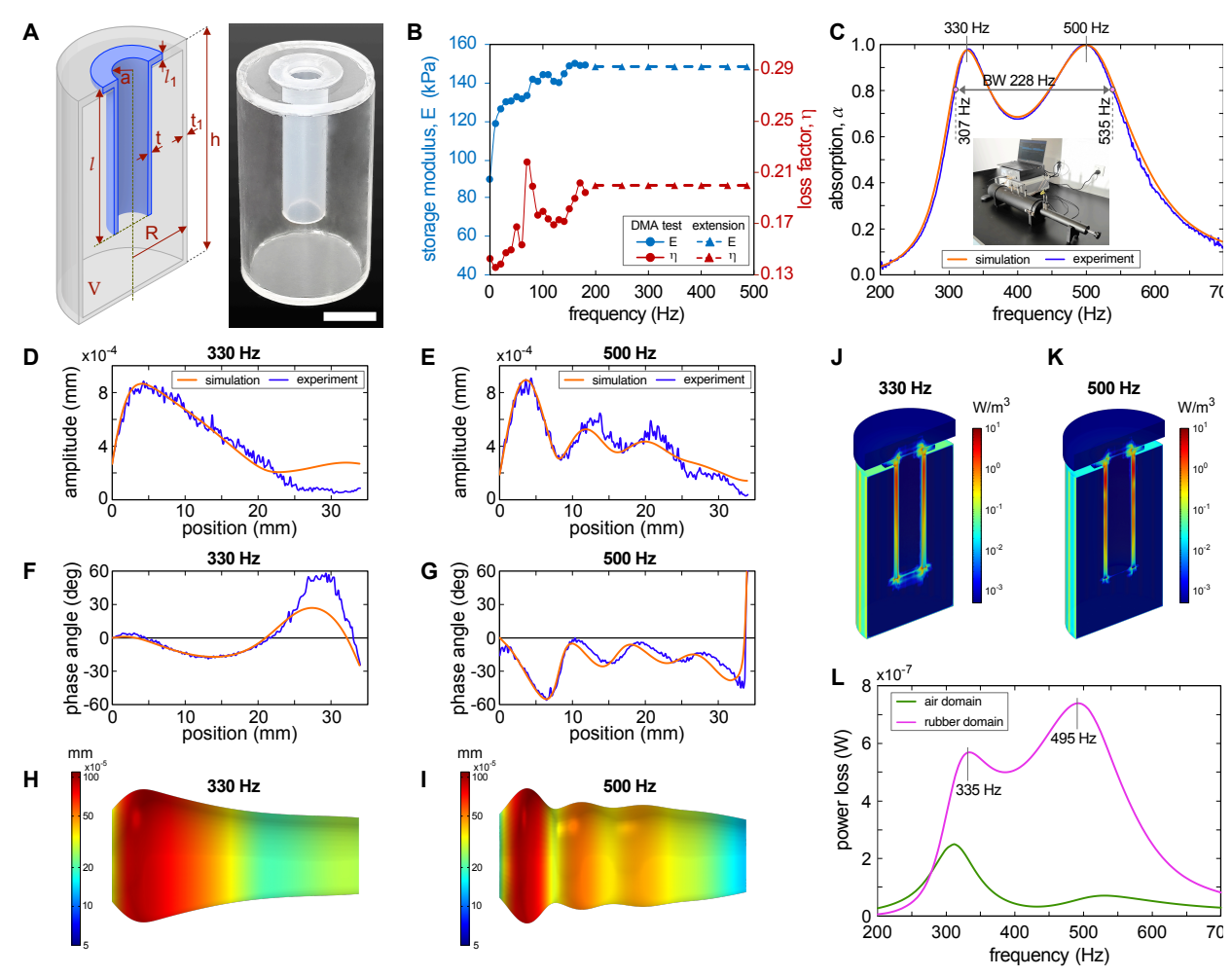


Fig. 2. Experimental and numerical characterization of a Flexible-Neck Helmholtz resonator. (A) Schematic (left) and photograph (right, white scale bar = 10 mm) of the resonator. Key dimensions: outer shell (R = 29 mm, h = 51.5 mm, $t_1 = 0.6$ mm), flexible neck (a = 4 mm, t = 1 mm, t = 36.5 mm, $t_1 = 1.5$ mm). (B) Frequency-dependent viscoelastic properties of Ecoflex-30 obtained from dynamic mechanical analysis (DMA). Solid lines represent experimental data (≤ 181 Hz), dashed lines represent extrapolated extension data (>181 Hz). (C) Measured (blue) and simulated (orange) sound absorption coefficient. (D–G) Axial surface displacement profiles: amplitude at (D) 330 Hz and (E) 500 Hz; phase angle at (F) 330 Hz and (G) 500 Hz. Experimental data (blue, measured using a laser Doppler vibrometer and averaged over data obtained in three axial lines at circumferential angles of 0° , 120° , 240°) align with simulation results (orange). (H, I) Simulated axisymmetric vibration modes (displacement magnified $\times 5000$ for visibility) at (H) 330 Hz and (I) 500 Hz. (J, K) Simulated dissipated power density distribution at (J) 330 Hz and (K) 500 Hz. (L) A comparison of dissipated power between material damping in rubber and thermo-viscous losses in air. Note: Simulations used a sound source pressure of 1 Pa; experimental displacement data in D and E were scaled to match this reference pressure.

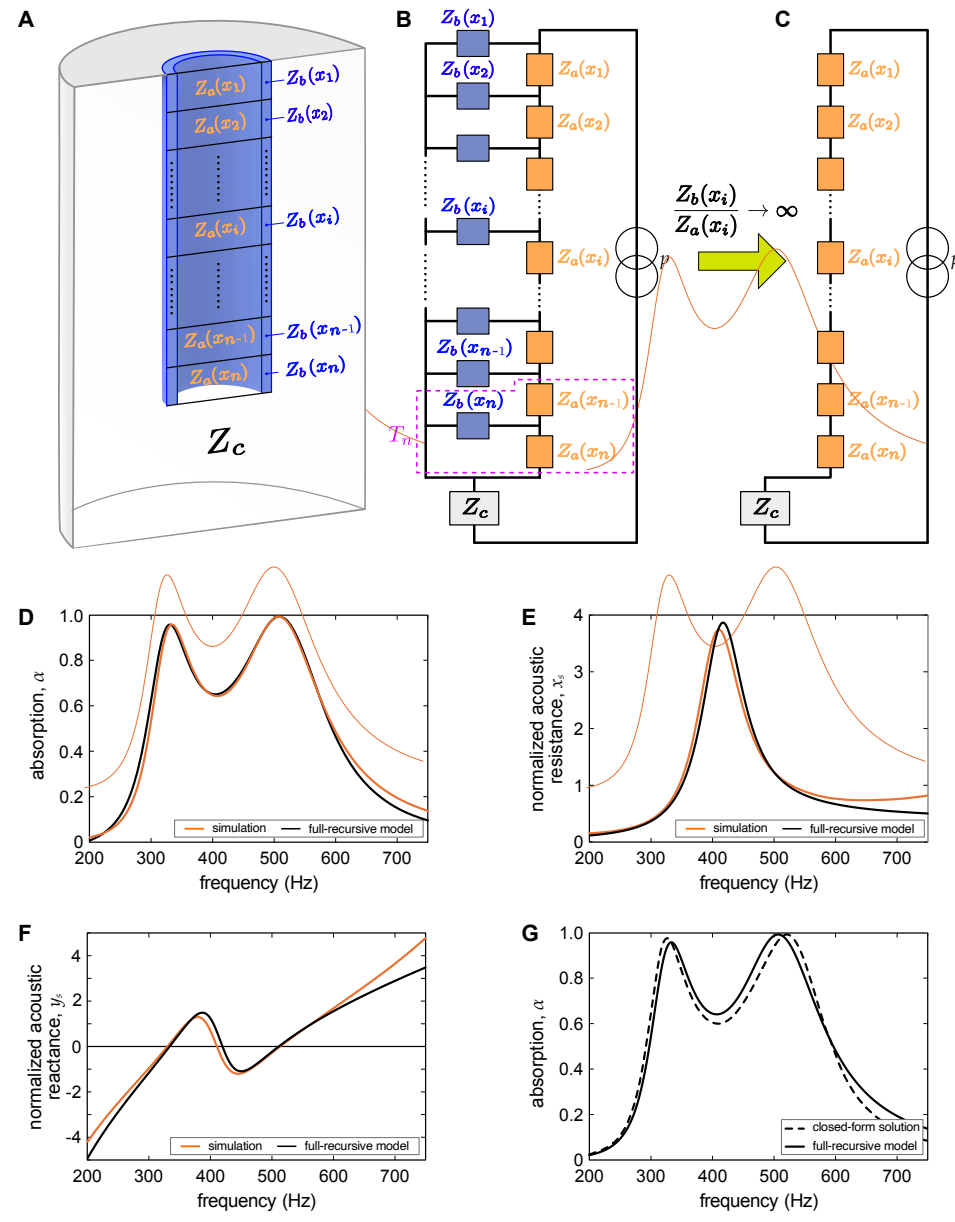


Fig. 3. Discretized equivalent impedance model for sound-structure interaction and its validation. (A) Schematic of the cylindrical shell and enclosed air column discretized into n equal length segments (length = l/n). For each segment i (i = 1,2,...,n), the acoustic impedance of the air column, $Z_a(x_i)$, and the equivalent acoustic impedance of the flexible shell, $Z_b(x_i)$, act in parallel, where $x_i = \frac{i}{n}l$ is the axial position of the i^{th} segment. (B) Equivalent acoustic impedance circuit of the full recursive model. (C) Reduced circuit for the rigid shell limit $(Z_b(x_i) \gg Z_a(x_i))$, where the $Z_b(x_i)$ branches are neglected. (D-F) Comparisons between theoretical predictions (using the full recursive model) and finite element simulations for (D) sound absorption coefficient α ; (E) normalized acoustic resistance x_s ; and (F) normalized acoustic reactance y_s . (G) A comparison of absorption coefficients calculated using the closed-form analytical model and the full recursive model.

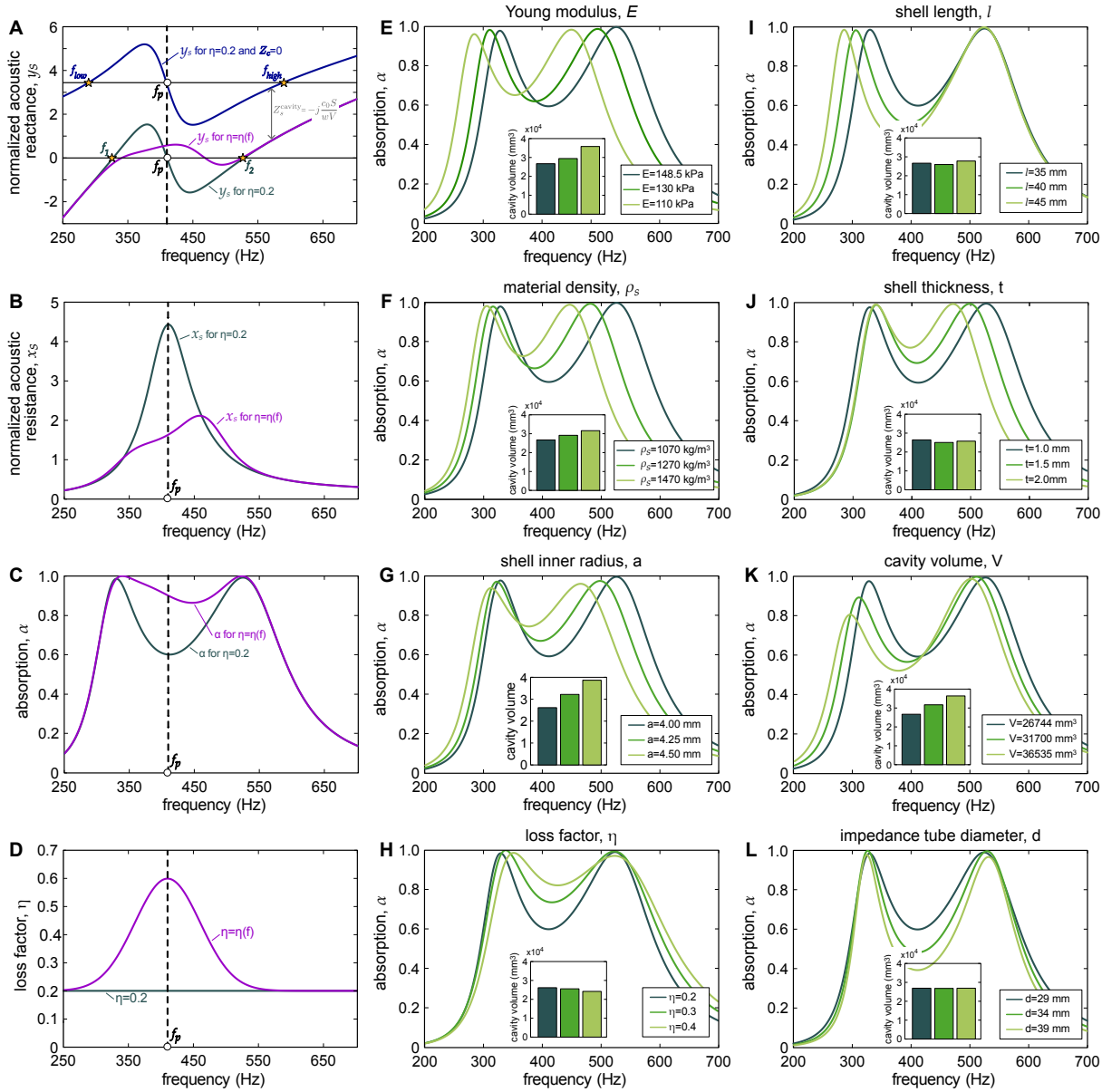


Fig. 4. Broadband tuning of sound absorption through impedance matching and parametric analysis. (A) Normalized acoustic reactance y_s . Baseline nonlinear coupling reactance (Im($Z_{couple}S/\rho_0c_0$), blue) exhibits a Z-shaped profile with inflection frequency f_p . Cavity reactance $Z_s^{cavity} = -j\frac{c_0S}{\omega V}$ (gray) shift y_s downward, creating three reactance zeros ($y_s = 0$) at f_1 , f_p , and f_2 (green). Frequency-selective loss modulation $\eta(f)$ (see D) flattens the Z-profile (purple). (B) Normalized acoustic resistance x_s . Low loss factor ($\eta = 0.2$) causes a pronounced peak at f_p (green). Frequency-selective damping $\eta(f)$ suppresses this peak, improving resistance matching (purple). (C) Absorption coefficients α . The baseline (green) shows a mid-frequency dip due to concurrent x_s and y_s deviations. Tuning through $\eta(f)$ eliminates the dip, achieving broadband absorption (purple). (D) Loss factor profiles: constant ($\eta = 0.2$, green) and

frequency-selective $\eta(f)$ peaking at f_p (purple). (E-J) Parametric effects on α (other parameters fixed; V co-adjusted per Eq.11 for optimal impedance matching): (E) Young's modulus E; (F) Material density ρ_s ; (G) Shell radius a; (H) Loss factor η ; (I) Shell length l; (J) Shell thickness t; (K-L) Parametric effects on α with isolated tuning: (K) Cavity volume V; (L) Impedance tube diameter d.

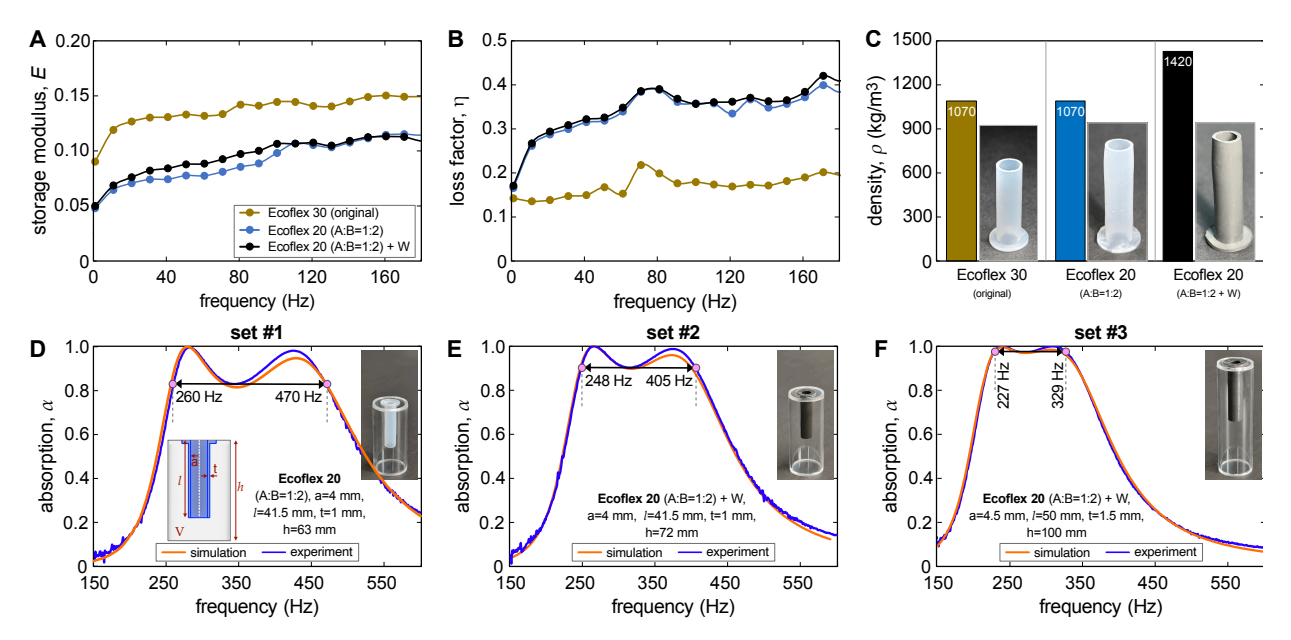


Fig. 5. Material optimization and customized absorber designs. **(A)** Frequency-dependent storage modulus E, **(B)** Frequency-dependent loss factor η , and **(C)** Material density ρ_s , for Ecoflex-30 (bronze), Ecoflex-20 (blue) and Ecoflex-20 + W (black). **(D-F)** Experimentally measured and simulated acoustic absorption coefficients for three resonator configurations: **(D)** Set 1 (Ecoflex-20; a = 4 mm, l = 41.5 mm, t = 1 mm, h = 63 mm). **(E)** Set 2 (Ecoflex-20 + W; a = 4 mm, l = 41.5 mm, t = 1 mm,